GPC: Recent developments

Bañas, Andrew Rafael; Kopylov, Oleksii; Villangca, Mark Jayson; Palima, Darwin; Glückstad, Jesper

Published in:
Optical Data Processing and Storage

Link to article, DOI:
10.1515/odps-2015-0002

Publication date:
2015

Document Version
Publisher's PDF, also known as Version of record

Review Article **Open Access**

Andrew Bañas, Oleksii Kopylov, Mark Villangca, Darwin Palima, and Jesper Glückstad*

GPC: Recent developments

DOI 10.1515/odps-2015-0002
Received March 11, 2015; accepted March 25, 2015

Abstract: Generalized Phase Contrast (GPC) is an efficient method for generating speckle-free contiguous optical distributions. It has been used in applications such as optical manipulation, microscopy, optical cryptography and more contemporary biological applications such as two-photon optogenetics or neurophotonics. Among its diverse applications, simple efficient shapes for illumination or excitation happen to have the biggest potential use beyond the research experiments. Hence, we preset recent GPC developments geared towards these applications. We start by presenting the theory needed for designing an optimized GPC light shaper (GPC LS). A compact GPC LS implementation based on this design is then used to demonstrate the GPC LS's benefits on typical applications where lasers have to be shaped into a particular pattern. Both simulations and experiments show ~80% efficiency, ~3x intensity gain and ~90% energy savings. As an application example, we show how computer generated hologram reconstruction can be up to three times brighter or how the number of optical spots can be multiplied threefold while maintaining the brightness. Finally, to demonstrate its potential for biomedical multispectral applications, we demonstrate efficient light shaping of a supercontinuum laser over the visible wavelength range.

1 Introduction

The ability to shape light for both fixed and programmable shapes has many applications in both research and industry. With the widespread use of lasers that lend themselves to efficient reshaping due to their spatial coherence, light's versatility is further increased. Hence, laser beam shaping based on photon efficient phase-only methods are extensively applied in research such as optical trapping, advanced microscopy or manipulation [1]. Light shaping is also finding its use in novel and exciting applications such as neurophotonics and two-photon optogenetics [2] which apply optical tools to neuroscience, and "atomtronics" [3], wherein optical potential distributions are used to arrange atoms to form electronic circuit analogs. Outside the laboratory, efficient light shaping is also desirable for applications such as laser machining, photolithography and video displays to name a few. These diverse applications would require light to be shaped in different ways. For example, the illuminated surfaces of spatial light modulators (SLMs), used in both optics research and consumer display projectors, have a rectangular form factor. A variety of shapes bounded by steep edges are desirable in laser cutting or engraving. In two-photon optogenetics research [4], one would like to selectively illuminate intricate patterns of dendrites or axons within neurons, preferably with minimal noise or speckles.

Despite the diverse shape demands, laser sources typically exhibit a Gaussian profile. Shaping a Gaussian beam with the commonly practiced simple hard truncation, i.e. amplitude modulation, is inefficient. For example, around 70% of the incident power can be lost when illuminating a rectangle with an expanded Gaussian beam [5, 6]. To complicate matters, this wasted power could contribute to device heating which can either shorten the device lifespan or require even more power if active cooling is employed. Besides the obvious disadvantages of inefficiency, the high price tag of advanced laser sources, such as pulsed or supercontinuum, used for multi-photon excitation, biophotonics or other state-of-the-art experiments also demands efficient use of available photons.

1.1 Photon efficient static light shaping

For static beam shaping, several solutions based on phase-only methods exist for efficiently transforming a Gaussian beam into rectangular, circular or other simple patterns. These include engineered diffusers, microlens arrays or homogenizers [7, 8], refractive mapping [9], diffractive optical elements (DOE) [10, 11] or phase plates [12, 13]. Engineered diffusers, microlens arrays and homogenizers work

Andrew Bañas, Oleksii Kopylov, Mark Villangca, Darwin Palima: DTU Fotonik, Dept. Photonics Engineering, Ørsted Plads 343, Technical University of Denmark, DK-2800 Kgs. Lyngby, Denmark, http://www.ppo.dk
***Corresponding Author: Jesper Glückstad:** DTU Fotonik, Dept. Photonics Engineering, Ørsted Plads 343, Technical University of Denmark, DK-2800 Kgs. Lyngby, Denmark, http://www.ppo.dk, E-mail: jesper.gluckstad@fotonik.dtu.dk

similarly by sampling an incident beam as a collection of beamlets that are then redirected to form an output shape. These approaches, however, are more suitable for incoherent light as the recombination of randomly phase shifted beamlets in coherent light would create interference effects [14], resulting in speckled or grainy output intensities. Refractive mapping operates using a similar principle but redirects rays without introducing random phase shifts, giving the transformed output beam a well-defined wavefront. DOEs or single phase plates using Fourier optics principles can directly transform a Gaussian to a sinc or Airy disk-like distribution which, in turn, becomes a top hat in the far field or after an additional lens [12]. The quality of the transformed beam depends on how well the sinc or Airy distribution is approximated, and is thus sensitive to the input Gaussian which contributes convolution effects that blur the edges of the shaped output.

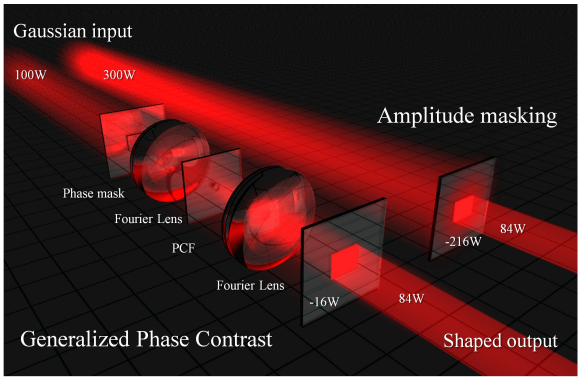

Figure 1: A GPC system efficiently transforming an incident Gaussian beam into a bright rectangle. Besides a standard imaging or telescopic 4*f* setup formed by the two Fourier lenses, GPC uses a simple binary phase mask at the input and phase contrast filter at the Fourier plane. An amplitude masking configuration is also shown to illustrate the significant difference in energy utilization when producing the same shaped output. (Figure adapted from [15])

Our proposed light shaping technique, the Generalized Phase Contrast method (GPC), belongs to a class of non-absorbing common path interferometers [16]. A phase-only aperture directly representing the desired output intensity is imaged through the interference of its high and phase-shifted low spatial frequencies. This is achieved by phase shifting the lower spatial frequencies through a phase contrast filter (PCF) at the Fourier plane (Fig. 1). GPC could thus be implemented with binary phase plates that are far simpler than those used by other Gaussian transformers as demonstrated in [17] with wet etched Pyrex, and as we shall also show in our experimental demonstrations. Binary phase plates are also easier to mass-produce with standard foundry processes common for silicon devices or microelectronics. When the phase mask and PCF are designed to give the same phase shift, both can even be fabricated from a single wafer. Unlike DOEs, GPC uses the target shape to directly interface with the incident Gaussian, instead of the target's Fourier transform. This makes GPC robust to input beam variations. The use of common path interferometry renders steep well-defined edges in the shaped output. Furthermore, the target output shapes could easily be replaced without increasing the fabrication complexity of the phase aperture or PCF. GPC's use of an imaging geometry also avoids dispersion effects which makes it advantageous for use with multiple wavelengths [18, 19] or temporal focusing [2, 4] which can effectively confine light along the axial direction.

1.2 Dynamic light shaping

Coupled with dynamic phase SLMs, the efficient generation of arbitrary light intensity patterns is also desirable. Applications include machine vision, optical trapping and manipulation, and two-photon optogenetics. Depending on the requirements, computer- holography (CGH) [20, 21] and GPC [22] are the main options for phase-only beam shaping. Computer-generated holography usually employs a focusing configuration, such that the output is the Fourier transform of light modulated by the SLM. This makes DH ideal for creating 2D or 3D spot arrays useful for optical tweezing [23] or photo stimulation at different planes [24]. A focusing geometry with a fixed illumination, however, is inherently prevented from generating contiguous light patterns desirable for some applications. Extended intensity patterns formed by aggregating spots with differing phase values and overlapping point spread functions thus results in speckles that resemble noise [25]. The intensity fluctuations in speckled extended intensity patterns become a problem when they are enhanced by two-photon excitation such as in direct laser writing [26] or in two-photon optogenetics [4].

With its advantage of contiguous, speckle-free patterns and computationally simple SLM encoding, GPC therefore finds uses in dynamic applications such as optical trapping and manipulation [1, 27, 28], and two-photon optogenetics [2]. Unlike speckled or discontinuous patterns, light distributions with contiguous intensity and phase remain localized while propagating enabling extended optical manipulation [1, 27, 29, 30]. Patterns formed by an imaging geometry are easily updated in real time giving more control when manipulating com-

plex 3D microstructures [1, 27] or allowing use in conjunction with other high speed techniques. GPC's use with high speed galvano scanning mirrors, for example, allows trapping of massive arrays (14x14 microbeads) [28].

1.3 Replacing amplitude modulation

In practice, GPC generated light distributions resemble that of simple amplitude modulation. Both are characterized by sharply outlined patterns with contiguous phase and intensity. However, these techniques are opposites when it comes to photon efficiency. GPC's photon efficiency is typically over ~80%. On the other hand, amplitude modulation typically has a low efficiency, directly proportional to the encoded pattern's fill factor and also dependent on the modulating device (e.g. LCoS or DMD).

Traditionally, GPC is used to transform top hat illumination into a plurality of intensity profiles [31]. Obtaining the initial top hat input, however, already removes a large fraction of the incident light unless employing another efficient beam shaping method like the ones mentioned earlier. Directly using Gaussian illumination for dynamic GPC applications is therefore an attractive alternative for economizing the available power in beam shaping experiments.

To compare with amplitude modulation, we consider GPC's efficiency and relative intensity gain. We also find it convenient to combine these two interdependent variables. Hence, we define the energy savings as the energy saved when replacing an amplitude masking system with a GPC system that gives the same brightness. This definition is illustrated in Fig. 2 where both light shaping techniques are used to deliver 84 watts within a rectangular region. While an 84% GPC system would require 100 W and lose 16 W, a 28% efficient hard truncated Gaussian would require 300 W and lose 216 W. Hence, using a GPC system saves 200 W or 93% of photon energy losses in a typical amplitude masking approach.

Mathematically, we thus define the energy savings as

$$\text{E. savings} = \left(1 - \frac{(100\% - \text{GPC eff}\,\%)}{(\text{GPC gain}) \times (100\% - \text{Amp masking eff}\,\%)}\right) \times 100\%. \quad (1)$$

We therefore use the energy savings as a metric to compare GPC with amplitude masking in our experiments.

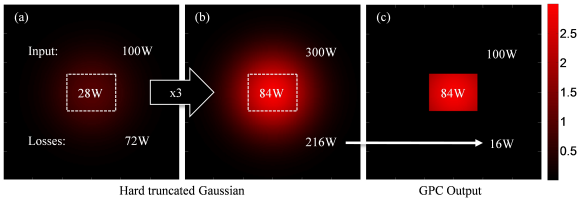

Figure 2: Comparison of GPC light shaping to a hard truncated Gaussian delivering 84 W on identical rectangular areas. Being only 28% efficient (a), the truncated Gaussian requires 300 W and loses 216W (b). The GPC light shaper requires only 100 W, saving 200 W (c) (Figure adapted from [6]).

2 GPC optimization

2.1 Optimizing GPC for output contrast

Below we present mathematical analysis of the $4f$ GPC setup depicted in Fig. 1. The field at the input plane can be described as

$$p(x, y) = a\,(x, y) \exp\left[i\phi\,(x, y)\right] \quad (2)$$

where $a(x,y)$ is an amplitude profile that arises due to the illumination beam and any limiting input aperture while $\phi\,(x, y)$ is the encoded phase modulation. The optical Fourier transform on the phase-encoded input light would then be located at the filter plane where the phase shifting PCF is applied. The transfer function of such PCF with a circular θ-phase shifting region has the form,

$$H(f_x, f_y) = 1 + [\exp(\mathrm{i}\theta) - 1]\,\mathrm{circ}\,(f_r/\Delta f_r) \quad (3)$$

where f_x, f_y and f_r are the abscissa, ordinate and radial spatial frequency coordinates, respectively. The associative groupings in Eqn. (3) are chosen to explicitly model how the filter generates a synthetic reference wave (SRW). The first term in the filter simply transmits all the Fourier components and, hence, projects an inverted copy of the input at the output plane. The second term is a low pass filter whose cutoff frequency, Δf_r, is the radius of the PCF's phase shifting region. At the output plane, the low-pass-filtered image of the input phase variations, scaled by a multiplicative complex factor, $[\exp(\mathrm{i}\theta) - 1]$, serves as a reference wave. Thus the synthesized intensity pattern at the output plane is formed from the interference of an inverted copy of the original input with its low passed version acting as the SRW

$$I\left(x', y'\right) \approx \left|o(x', y')\right|^2 = \left|a\left(x', y'\right) \exp\left[i\phi\left(x', y'\right)\right] + [\exp(i\theta) - 1]\,\overline{a}g\left(x', y'\right)\right|^2. \quad (4)$$

Here, we have used an approximation for the SRW, $[\exp(i\theta) - 1]\,\overline{\alpha} g\left(x', y'\right)$ [5], where the spatial profile $g\left(x', y'\right)$ is the low passed version of the unmodulated input light

$$g(x', y') = \Im^{-1}\left\{\mathrm{circ}\left(f_r/\Delta f_r\right)\Im\left\{a(x, y)\right\}\right\} \tag{5}$$

scaled by the strength of the normalized zero$^{\text{th}}$ order, $\overline{\alpha}$, that would take input phase modulations into account

$$\begin{aligned}\overline{\alpha} &= |\overline{\alpha}|\exp(i\phi_{\overline{\alpha}}) \\ &= \iint a(x, y)\exp[i\phi(x, y)]dxdy \Big/ \iint a(x, y)dxdy\end{aligned} \tag{6}$$

On the optical axis, optimal contrast in the interferogram is thus obtained when the two terms in Eqn. (4) have matching amplitudes [5], which is satisfied when

$$2g(0, 0)\,|\overline{\alpha}|\,\left|\sin\left(\theta/2\right)\right| = 1. \tag{7}$$

2.2 GPC with Gaussian illumination

To proceed with our analysis we set the illumination to follow a radially symmetric Gaussian profile with a $1/e^2$ waist, w_0

$$a(r) = \exp\left(-r^2\Big/w_0^2\right). \tag{8}$$

To simplify our analysis, we would, for now, assume that the phase mask is circular. We also assume that both the input phase mask pattern and PCF impart π-phase shifts on the transmitted light. When evaluating Eqn. (5), we note that $g(r')$ is a Fourier transform of a truncated Gaussian. Evaluating this Fourier transform is not straightforward, thus different approximations have been presented in the literature [32]. Nonetheless, the central value can be obtained analytically

$$\begin{aligned}g\left(r' = 0\right) &= \Im^{-1}\left\{\mathrm{circ}\left(f_r/\Delta f_r\right)\pi w_0^2\exp(-f_r^2/w_f^2)\right\} \\ &= 1 - \exp(-\eta^2).\end{aligned} \tag{9}$$

Here, we have defined η as the ratio of the PCF phase shifting radius, Δr_f, to the Gaussian waist at the Fourier plane, w_f, when the wavelength is λ and the focal length is f.

$$\eta = \Delta r_f/w_f = \Delta r_f\pi w_0/(\lambda f) \tag{10}$$

For a π-phase shifting circular phase mask with radius Δr, the modulated input could be expressed as

$$a(r)\exp\left[i\phi(r)\right] = \exp\left(-r^2\Big/w_0^2\right)\left[1 - 2\mathrm{circ}\left(r/\Delta r\right)\right]. \tag{11}$$

Since this also involves a truncated Gaussian, the evaluation of $\overline{\alpha}$ is similar to $g(r'=0)$

$$\overline{\alpha} = 2\exp(-\zeta^2) - 1 \tag{12}$$

where we defined the dimensionless ζ as the ratio between the phase mask radius and input Gaussian waist,

$$\zeta = \Delta r/w_0. \tag{13}$$

On the optical axis, optimal contrast in the interferogram is thus obtained when the two terms in Eqn. (4) have matching amplitudes [5]. Hence, we can express Eqn. (7) using Eqn. (9) and (12) giving the condition for optimal contrast

$$\left[2\exp(-\zeta^2) - 1\right]\left[1 - \exp(-\eta^2)\right] = 1/2. \tag{14}$$

Although this derivation is for a circular phase mask, extending to any shape is a matter of finding the corresponding $\overline{\alpha}$. This can also be analytically derived for rectangular phase masks as we would later show, but in many cases involving arbitrary geometries, $\overline{\alpha}$ would have to be obtained via numeric integration.

2.3 Optimizing GPC for photon efficiency

For a beam shaping system, efficiency (eff) is measured as the energy within the target output shape, S, divided by the overall incident energy,

$$\text{GPC eff} = \iint_S I(x, y)\,dxdy \Big/ \iint a^2(x, y)\,dxdy. \tag{15}$$

Since the exact analytic form of the intensity is not readily available, we take a different approach where we look for phase mask and PCF configurations correlated with what is numerically found to be the most efficient (Fig. 3(a)). We find that efficiency is maximized when the first zero crossing of the Fourier transform coincides with the PCF radius, Δf_r. Conceptually, this could be understood by working backwards, starting with the desired output shape of a GPC system. The region from the filter plane to the output plane can be treated as a $2f$ focusing geometry like in Fourier holography. Hence, if a circular output is desired, this means, that the filter plane should look like an Airy disk-like function (green plot in Fig. 3(b)). When we now consider GPC's input plane, light outside of the desired shape, i.e. the peripheral Gaussian envelope, would perturb the central part of the desired Airy-like distribution at the filter plane. These low frequency perturbations reemerge at the output as light outside the desired shape.

With an idea of how the Fourier distribution should look like, we thus adopt an optimization method similar to how CGH applies phase constraints to get a desired Fourier transform output [33], or how matched filtering GPC uses concentric rings to emulate plane wave focusing and, consequently, output focal spots [34]. For the circular pattern, the deviations from the ideal Airy-like function are minimized when the PCF's radius coincides with the zero crossing at the central region at the Fourier plane. Applying a π-phase shift within this region inverts the sign of the low frequencies, making the Fourier distribution more similar to the desired Airy-like function.

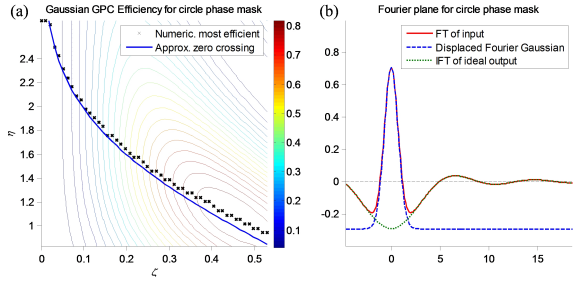

Figure 3: (a) Color contour plot of numerically obtained efficiency as a function of (ζ, η). The black crosses mark the highest efficiency for a given ζ. The blue plot corresponds to our condition for the PCF radius to coincide with the first zero crossing of the Fourier transform. (b) The Fourier transform of the phase-only aperture (red plot) can be approximated with a displaced Gaussian (blue plot) near the PCF phase shifting region. The inverse Fourier transform of the ideal output (green plot) is also shown for reference. (The x and y axes are normalized to w_f and πw_0^2 respectively.) (Figure adapted from [6]).

To obtain a simplified analytic expression for this efficiency condition, we assume that the Airy disk function has a negligible curvature within the phase shifting region, $f_r \leq \Delta f_r$. At this region, the Fourier transform of Eqn. (11) is approximately

$$\begin{aligned}&\Im\left\{\exp\left(-r^2/w_0^2\right)\left[1-2\mathrm{circ}\left(r/\Delta r\right)\right]\right\}\\&\approx \pi w_0^2\left\{\exp\left(-f_r^2/w_f^2\right)-2\left[1-\exp\left(-\zeta^2\right)\right]\right\}\end{aligned} \tag{16}$$

This is illustrated in Fig. 3(b), where the displaced Gaussian (blue plot), approximates the Fourier transform (red plot) at low frequencies. To make the PCF radius coincide with the first zero crossing, we thus impose

$$\exp\left(-\eta^2\right)-2\left[1-\exp\left(-\zeta^2\right)\right]=0. \tag{17}$$

2.4 Optimizing contrast and efficiency

Solving for ζ and η from Eqn. (14) and (17) gives us the optimal parameters for a circular phase mask

$$\zeta=\sqrt{\ln\left[\frac{2}{1+\sqrt{1/2}}\right]}=0.3979, \tag{18}$$

$$\eta=\sqrt{-\ln\left\{2\left[1-\exp\left(-\zeta^2\right)\right]\right\}}=1.1081. \tag{19}$$

Numerically evaluating the GPC output from this ζ-η pair gives an efficiency of ~84% and a gain of ~3x relative to the input Gaussian's central intensity (see Table 1). To generalize to arbitrary shapes Eqn. (18) and (19) can be expressed in terms of $\overline{\alpha}$ instead of ζ, giving

$$\overline{\alpha}=\sqrt{1/2}=0.7071, \tag{20}$$

$$\eta=\sqrt{-\ln\left(1-\sqrt{1/2}\right)}=1.1081. \tag{21}$$

These two equations summarize the conditions for an optimally performing GPC system under Gaussian illumination. The phase mask's geometry is embodied in $\overline{\alpha}$, which can be tweaked in different ways such that Eqn. (20) is satisfied. The fixed value for η in Eqn. (21) means that a reconfigurable GPC system with a fixed PCF will still perform optimally with different phase masks satisfying Eqn. (20). The succeeding sections use these two equations to optimize Gaussian GPC with rectangular and arbitrary patterns.

2.5 Extending to rectangular apertures

Gaussian illumination encoded with a π-phase shifting rectangle with dimensions $W\times H$ can be expressed as (*cf.* Eqn. (11))

$$\begin{aligned}&a\left(x,y\right)\exp\left[i\phi\left(x,y\right)\right]\\&=\exp\left[-\left(x^2+y^2\right)/w_0^2\right]\left[1-2\mathrm{rect}\left(x/W\right)\mathrm{rect}\left(y/H\right)\right].\end{aligned} \tag{22}$$

To optimize a GPC system using rectangular phase apertures, we first identify $\overline{\alpha}$. Using Eqn. (22) to evaluate Eqn. (6)

$$\begin{aligned}\overline{\alpha}&=\frac{\pi w_0^2-2\pi w_0^2\mathrm{erf}\left(\frac{W/2}{w_0}\right)\mathrm{erf}\left(\frac{H/2}{w_0}\right)}{\pi w_0^2}\\&=1-2\mathrm{erf}(\zeta_{\mathrm{Rect}}\mathrm{erf}(\zeta_{\mathrm{Rect}}/A_R)).\end{aligned} \tag{23}$$

Here we defined the aspect ratio, $A_R = W/H$ and ζ_{Rect} for rectangular phase apertures as half the width divided by

the input Gaussian waist, $\zeta_{\text{Rect}} = W/2w_0$. There is no direct way for solving ζ_{Rect} to get $\overline{\alpha}$ using Eqn. (23), except for a square, $A_R = 1$, which gives

$$\zeta_{\text{Rect}} = \text{erf}^{-1}\left(\sqrt{\frac{1-\sqrt{1/2}}{2}}\right) = 0.3533. \quad (24)$$

For other aspect ratios, ζ_{Rect} can be found numerically or by graphically looking for the intersection of the plots of the following equations obtained by modifying Eqns. (14) and (17) with the $\overline{\alpha}$ for rectangles.

$$\left[1-\exp\left(-\eta^2\right)\right]\left[1-2\text{erf}\left(\zeta_{\text{Rect}}\right)\text{erf}\left(\zeta_{\text{Rect}}/A_R\right)\right] = 1/2, \quad (25)$$

$$\exp\left(-\eta^2\right) - 2\text{erf}\left(\zeta_{\text{Rect}}\right)\text{erf}\left(\zeta_{\text{Rect}}/A_R\right) = 0. \quad (26)$$

Figure 4 shows the plots of Eqn. (25) in solid lines and Eqn. (26) in dashed lines. A_R is chosen from common video display aspect ratios. The plot is zoomed at the intersections which occur at $\eta = 1.1081$. The numeric values of ζ_{Rect} at these intersections are listed in Table 1 (to 4 decimal places).

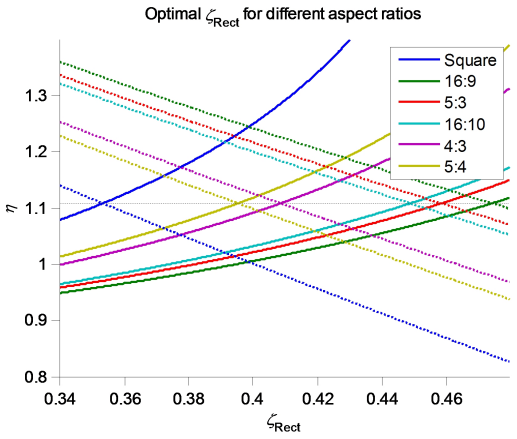

Figure 4: Optimal ζ_{Rect} for rectangular phase masks with different aspect ratios are found where the solid (Eqn. 25) and dashed lines (Eqn. 26) with the same color intersect, or where either of these lines intersect with $\eta = 1.1081$ (Figure adapted from [6]).

3 Numerical experiments

3.1 Circular and rectangular phase apertures

Numerical calculations for a circle and different rectangular aspect ratios are summarized in Table 1. These results were obtained using an 8192×8192 sample FFT with $w_0 = 240.7957$ samples such that Δf_r is an integer value, $\eta w_f = 12$ samples. GPC efficiency is defined as in Eqn. (15) and the gain is defined as the central intensity at the output (input central intensity is unity). Since discretization errors prevent ζ or ζ_{Rect} from being represented accurately, we also list their effective values when integer rectangle sizes are used.

Figures 5(a)-(c) shows GPC output for a circle, square and a rectangle with 16:10 aspect ratio using optimized parameters listed in Table 1. The corresponding efficiencies, gain and energy savings are also shown for each shape. The corresponding line scans are shown in Figures 5(d)-(e).

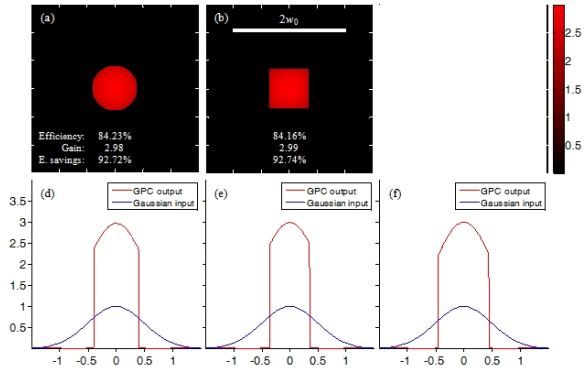

Figure 5: GPC intensity outputs for circle (a), square (b), rectangle (c). The scale bar in (b) is twice the $1/e^2$ Gaussian waist, and tick marks in (a)-(c) are separated by half the Gaussian waist. Efficiencies, gain and energy savings are also shown, and are consistently ~84%, ~3x and ~93% respectively. The corresponding intensity line scans are shown in (d)-(f). The x-axis is normalized to w_0 (Figure adapted from [6]).

3.2 Arbitrary intensity patterns

3.2.1 Optimally scaled arbitrary patterns

Gaussian-illuminated GPC need not be constrained with patterns that can be dealt with analytically. In fact, it works best with arbitrary patterns that have high spatial frequencies, thus diverting light from the Fourier zero order, and reinforcing the validity of the Eqn. (20) and (21). Instead of analytically convenient circle or rectangle functions, we consider an arbitrary binary bitmap image, $b(x, y)$, having values 0 and 1, as our aperture. Assuming the binary image is mapped to 0 and π phase shifts on an incident Gaussian, we can numerically evaluate $\overline{\alpha}$ and scale

Table 1: Efficiency, intensity gain and energy savings of GPC shaped light compared with a hard truncated or amplitude masked Gaussian for a circle and different rectangles.

Shape or aspect ratio	ζor ζ_{Rect}	Effective ζor ζ_{Rect}	GPC eff (%)	GPC gain	Amp masking eff (%)	E. savings (%)
Circle	0.3979	0.3987	84.23	2.9751	27.20	92.72
Square	0.3533	0.3530	84.16	2.9884	27.02	92.74
5:4	0.3954	0.3945	84.11	2.9967	26.91	92.74
4:3	0.4087	0.4070	83.57	3.0060	26.71	92.54
16:10	0.4491	0.4485	83.61	3.0017	26.70	92.55
5:3	0.4587	0.4568	84.03	3.0155	26.61	92.78
16:9	0.4745	0.4734	84.05	3.0162	26.58	92.80

$b(x, y)$ such that

$$\overline{\alpha} = 1-2\left\{\iint b(x,y)\exp[-(x^2+y^2)/w_0^2]\right\}/\pi w_0^2 = \sqrt{1/2}. \tag{27}$$

In our simulations we first start with a large bitmap and optimize w_0 which is easier to change. Once Eqn. (27) is satisfied, we revert to the original w_0 and then scale the image preserving its optimal proportion with w_0. Results for various optimized patterns are shown in Fig. 6.

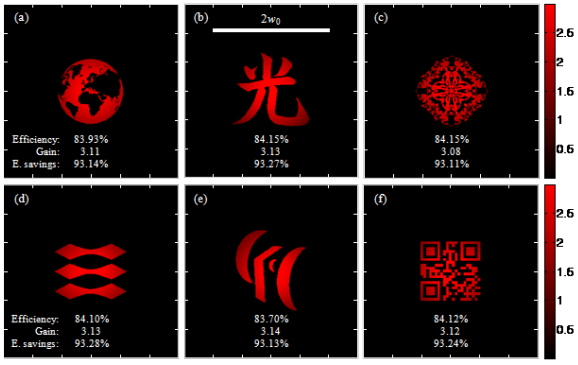

Figure 6: Intensity profiles of various arbitrary shapes scaled to satisfy Eqn. (21). Corresponding efficiencies, gain and energy savings are also shown, and are consistently ~84%, ~3x and ~93% respectively (Figure adapted from [6]).

3.2.2 Dynamic and arbitrarily sized excitation patterns

In dynamic experiments, scaling the light pattern is often not an option. Such restriction usually applies when light has to interact with manipulated objects or biological samples. Nonetheless, it is possible to keep $\overline{\alpha}$ optimal by addressing an additional outer phase ring such that Eqn. (20) or (27) is still satisfied. This is similar to what is done in [2] for top hat illuminated GPC. Hence, given an arbitrary bitmap, b, the inner radius of the compensating ring could be found,

$$R_{\mathrm{comp}} = w_0 \times \left(-\ln\left[\left(1/2-\sqrt{1/8}\right) - \left\{\iint b(x,y)\exp\left[-\left(x^2+y^2\right)/w_0^2\right]dxdy\right\}/\pi w_0^2\right]\right)^{1/2}. \tag{28}$$

Results for ring compensated neuron shaped patterns are shown in Fig. 7. Figures 7(d)-(f) show the possibility to optimally illuminate a cell that is branching out. We observe that the gain tends to be higher with a less efficiency-optimized GPC setup. This counteracting behavior of intensity gain and photon efficiency helps to keep the energy savings at around ~85-93%.

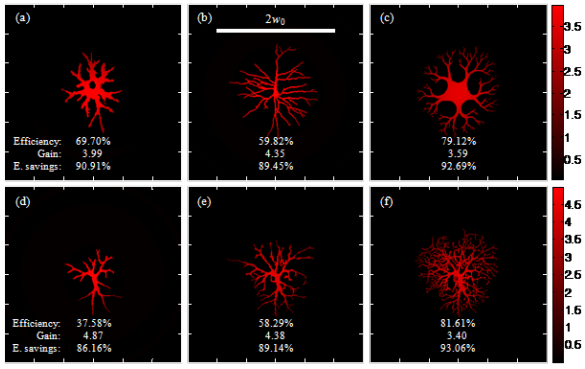

Figure 7: (a)-(c) Intensity profiles of various neuron-inspired shapes, directly drawn without scaling, but α-compensated by an outer phase ring. (d)-(f) Intensity profile for a pattern that is branching out. Whereas the efficiencies and intensity gains are highly pattern dependent, the energy savings stays at around ~90% (Figure adapted from [6]).

3.3 Tolerances of some critical parameters

The numerical simulations presented did not consider experimental variables such as alignment, dirt, nonlinearities and other variations. Such variations, however, are always present in an actual experiment. There are arguably countless parameters to consider in a real setup, but among them, the PCF is the one with little room for error. The size of both the PCF and the Fourier focal spot are typically in the micron range. Misaligning these two beyond a certain extent effectively reverts a GPC phase imaging system to a normal $4f$ telescopic setup. Away from the zero order, the PCF phase shifts a smaller fraction of the light distribution that is not enough to form an effective SRW. We consider here the tolerances of some parameters that will be crucial in our experiments and current fabrication process, namely, the PCF's displacement and the effective phase shift of the phase mask and PCF.

3.3.1 PCF displacements

We numerically simulate typical PCF misalignment situations, i.e. axial displacements along the optical axis, and lateral displacements along the Fourier plane, assuming a compact GPC light shaper (GPC LS) designed for λ = 750 nm, $2w_0$ = 1 mm, and with f = 50 mm Fourier lenses. The input phase mask shapes considered are a circle, a square and a rectangle with 4:3 aspect ratio. Efficiencies and energy savings are evaluated at different displacements (Fig. 8). To anticipate other experimental parameters, the displacements are also expressed relative to the PCF size or focal length.

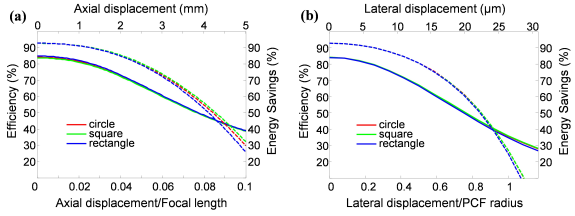

Figure 8: Tolerance of the PCF's positioning. The efficiency (solid lines) and energy savings (broken lines) are evaluated at different axial (a) and lateral (b) displacements (Figure adapted from [15]).

Along the axial direction, the efficiency stays at above 80% if the PCF does not go beyond ~2% of the focal length (~1.2 mm). Energy savings is slightly more robust allowing about ~2.5 mm axial displacement before the 80% cutoff. Lateral displacements are more sensitive owing to the size of the PCF. For the GPC LS considered (PCF radius = 26.5 μm), PCF displacements can go up to ~5 and ~12 microns before the efficiency and energy savings respectively go below 80%.

3.3.2 Phase mask and PCF phase shift variations

We also consider the effect of errors in the phase shift of the input phase mask and PCF that may arise e.g., due to etch rate-dependent fabrication process, such as in wet etching, where some deviations are to be expected. The evaluated efficiency and energy savings for different shapes showed very subtle differences so we only show the results for a 4:3 rectangular phase mask (Fig. 9).

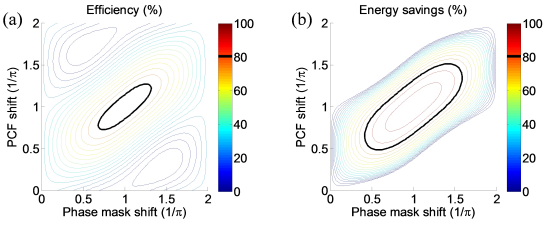

Figure 9: Contour plots showing the efficiency (a) and energy savings (b) of a GPC LS using a 4:3 rectangular phase mask. A black contour line is drawn around the region for which efficiency or energy savings are at least 80% (Figure adapted from [15]).

The diagonal region of favorable efficiency and energy savings shows that phase errors will have lower impact when both phase mask and PCF have the same phase shift (a similar result has also been derived for plane-wave illuminated GPC [35]). Hence, we can minimize deviations from optimal GPC performance by simultaneously etching the phase mask and PCF on the same wafer. The 80% cutoff regions bounded by the black contour lines in Fig. 10 show that phase shift variations of up to ~20% are tolerable for efficiency and up to 50% tolerance for energy savings.

4 Light shaping experiments

To verify our theoretical formulations and numerical simulations, we now demonstrate compact implementations of GPC for creating practical illumination shapes. Practical issues such as calibration of the PCF's axial position shall also be discussed. Using a dynamic spatial light modulator, we also show simple and efficient beam shaping of reconfigurable shapes geared towards materials process-

ing, biophotonics research and other contemporary applications. Our demonstrations are designed for specific wavelengths and input beam size thus using an optimized phase mask and PCF. Implementations that allow more input freedom, however, have also been demonstrated recently [36, 37] and were achieved with an adaptive PCF. Our light shaping experiments give ~80% efficiency, ~3x intensity gain, and ~90% energy savings which are in good agreement with the theoretical estimations. With such results, a GPC LS can be useful for industrial or commercial applications [15].

4.1 Calibration using a darkness phase mask

Experimental calibration and alignment are usually guided by some output metric. Normally, GPC is configured to have constructive interference at the foreground. However, measuring the optimal brightness requires setting a reference. By changing the foreground's fill factor relative to the Gaussian illumination, GPC can also generate darkness at the output via destructive interference. For a π-phase shifting circle phase mask, we found numerically that darkness is generated when the phase mask radius is ~1.02 times the Gaussian $1/e^2$ radius. It also works with a truncating iris, which generates darkness at an aperture radius of about ~0.83w_0. Although a truncating iris has the advantage of being wavelength independent, it is much easier to work with a transparent phase-only darkness mask as peripheral light guides proper alignment. Furthermore, a phase mask can be fabricated on the same wafer with the other input phase masks and PCFs, making it economical. For dynamic experiments, this means that the SLM can be used directly for calibration without adding extra components. Figure 10(a)-(b) shows GPC simulations using a darkness phase mask. Successfully reproducing this experimentally, as shown in Fig. 10(c) indicates that the components have been properly aligned and calibrated. Hence, the succeeding GPC experiments presented here used this calibration technique to precisely adjust the PCF's position.

4.2 Static light shaping experiments

4.2.1 Construction of a pen sized GPC LS

For our static beam shaping experiments, we designed and constructed a GPC LS that interfaces directly with the output of laser sources. Commercial lasers typically have

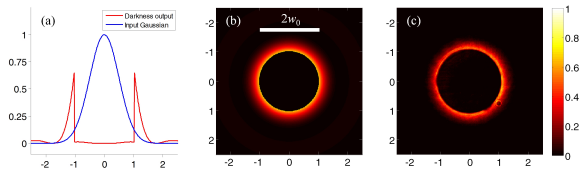

Figure 10: Relative intensity of a GPC generated darkness compared to the input Gaussian (a). Intensity profiles obtained from a simulation (b) and from experiment (c) (Figure adapted from [15]).

beam diameters of around ~1mm to ~5mm. Using two f = 50 mm Fourier lenses allowed us to keep the setup compact. This also kept the PCF at a size that is still manageable with wet etching and off-the-shelf optics assembly. The GPC LS assembled with Thorlabs's half-inch optics and 16mm cage system is shown in Fig. 11. Its overall length is a little over $3f$ = 150 mm, which is around the size of a pen. For more compact implementations, such as for OEM use, integrated micro-optics platforms [38] or alternative fabrication and assembly techniques can also be adopted.

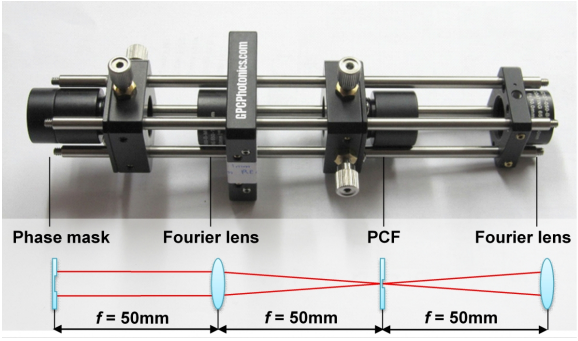

Figure 11: Pen sized GPC LS using two f =50 mm Fourier lenses and half inch optics assembly. (Figure adapted from [15]).

We designed the phase mask and PCF for use with $2w_0$ = 1 mm, λ = 750 nm and f = 50 mm. The material used is fused silica (n = 1.454 at λ =750 nm). The PCF radius is calculated using Eqns. (10) and (21), hence,

$$\Delta r_f = \eta \frac{\lambda f}{\pi w_0} = \frac{1.1081 \times 0.75\mu m \times 50mm}{\pi \times 0.5mm} = 26.5\mu m \tag{29}$$

The etch depth was determined such that it gives a half-wavelength optical path difference relative to the unetched surroundings and can be found using the following equation:

$$\text{etch depth} = (\lambda/2)/(n-1). \tag{30}$$

Hence we used an etch depth of ~826 nm. Conventional UV-lithography followed by wet etching in a buffered HF (BHF) was used to form the patterns

For a circle or for rectangles, the phase mask size relative to the Gaussian beam diameter can be obtained from the tabulated ζ or ζ_{Rect} values in Table 1. As an example, a rectangular phase mask with aspect ratio 4:3, the width has to be 0.4087 (ζ_{Rect}) times the beam diameter.

$$W = \zeta_{\text{Rect}} \times (2w_0) = 0.4087 \times 1\text{mm} = 408.7\mu\text{m} \qquad (31)$$

From a four inch wafer, the phase masks and PCFs are diced such that they can be fitted into half-inch optics mounts. The size of the circular and square phase masks are obtained in a similar manner. The ζ or ζ_{Rect} for the phase masks used are included on Table 2, together with the summary of experimental results. During assembly, we utilized the phase-only darkness calibration masks to fine tune the axial placement of the PCF. These masks were fabricated with a radius of 510 µm.

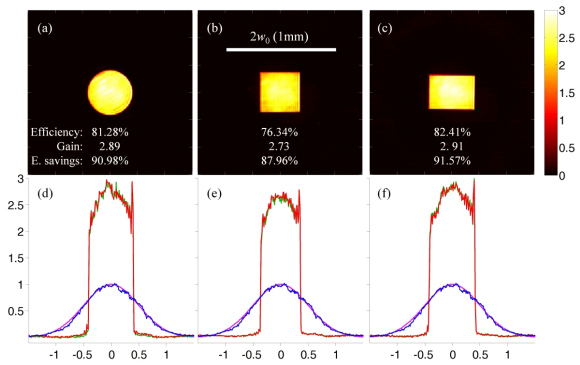

Figure 12: GPC intensity outputs from experiments for a circle (a), a square (b), and a 4:3 rectangle (c) phase mask. The scale bar in (b) is twice the $1/e^2$ Gaussian waist, and tick marks in (a)-(c) are separated by half the Gaussian waist. Efficiencies, gain and energy savings are also shown, and are consistently around ~80%, ~3x and ~90% respectively. The corresponding GPC intensity line scans are shown as green and red traces in (d)-(f) together with intensity line scans when simply imaging the Gaussian beam (blue). The axes are normalized relative to the Gaussian fit (magenta) and tick marks are spaced $w_0/2$ (0.25mm) apart (Figure adapted from [15]).

4.2.2 Static light shaping results

For our laser source, we used a supercontinuum laser from NKT Photonics that has a 1mm beam diameter. This enables us to conveniently test different wavelengths by inserting a color filter, instead of replacing the entire laser. In our measurements, we used a 750 nm bandpass filter from Thorlabs with a bandwidth of 10 nm. This laser source is directed to the GPC LS using some relay mirrors that also provided beam alignment. Output from the GPC LS is magnified (2x) then captured by a beam profiler (Gentec-EO).

Different GPC output shapes were tested on the same GPC LS by interchanging the input phase masks. To rule out reflection losses, we used a reference Gaussian that is obtained when the PCF is misaligned and the phase mask is removed. The efficiency, gain and energy savings results are summarized in Table 2.

Figures 12 (a)-(c) show GPC outputs for a circle, a square and a rectangle with 4:3 aspect ratio using optimized parameters listed in Table 1. The corresponding efficiencies, gain and energy savings are also shown for each shape and are consistently around ~80%, ~3x and ~90% respectively. The corresponding line scans are shown in Figs. 12 (d)-(e). Two output measurements were taken (red and green plots) and measured against the reference Gaussian (blue plot). A Gaussian fit (magenta) is used to normalize the axes in Fig. 12. There is an observable intensity roll off in the GPC output, but this is flatter than what can be attained from a hard truncated Gaussian [5]. If a flatter intensity is critical, a phase mask with an intensity compensating curvature [39] may be used with the GPC LS.

4.3 Arbitrary patterns formed with a dynamic phase-only spatial light modulator

We now show how GPC is applied for dynamic light shaping of speckle-free contiguous patterns. The setup used for generating arbitrary GPC output shapes is shown in Fig. 13.

We used a phase-only SLM (Hamamatsu Photonics) that has an area of 16×12 mm^2 and pixel pitch of 20 microns. The SLM was illuminated with a 532 nm diode laser module (Odicforce), horizontally polarized and expanded such that $2w_0$ = 4 mm (200 SLM pixels). The Fourier lens used has a focal length of 100mm. Here, we used a PCF with Δr_f = 9.4 µm which is relatively small due to the larger area of the SLM. The etch depth was ~577 nm in fused silica (n = 1.46 at λ =532 nm). When a compact footprint is not crucial, longer focal lengths can be used to minimize the focused light-intensity at the PCF. The resulting dynamic patterns are captured with a CCD camera (JAI TM-1327GE).

4.3.1 Optimally scaled arbitrary patterns

Binary bitmap images, $b(x, y)$, were displayed on the SLM and mapped to 0 and π phase shifts. These images were

Table 2: Experimentally measured efficiency, intensity gain and energy savings of GPC shaped light compared with a hard truncated or amplitude masked Gaussian for a circle and different rectangles.

Shape or aspect ratio	ζor ζ_{Rect}	Width or Diameter (μm)	GPC eff (%)	GPC gain	Amp masking eff (%)	E. savings (%)
Circle	0.3979	397.9	81.28	2.89	28.15	90.98
Square	0.3533	353.3	76.34	2.73	27.97	87.96
4:3	0.4087	408.7	82.41	2.91	28.31	91.57

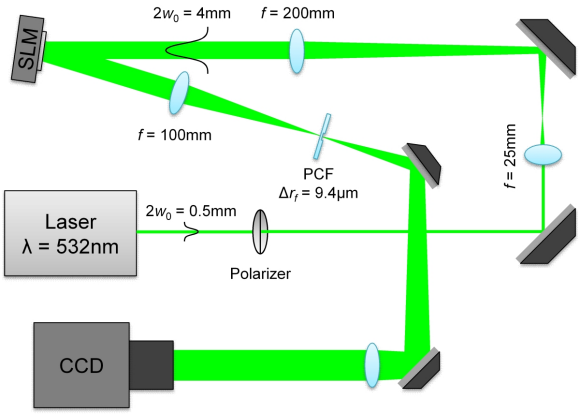

Figure 13: GPC LS setup with Gaussian illumination on a dynamic spatial light modulator (SLM). The SLM is illuminated with horizontally polarized Gaussian beam ($2w_0 = 4$ mm). The phase-modulated beam enters the GPC system ($f = 100$mm and $f = 150$ mm Fourier lenses) whose output is imaged onto a CCD camera (Figure adapted from [15]).

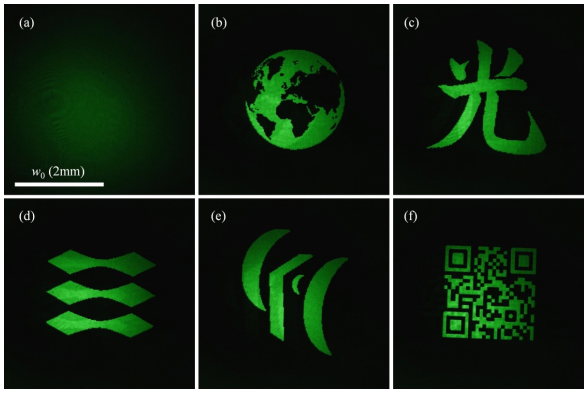

Figure 14: GPC generated arbitrary patterns obtained from experiments. The patterns are optimally scaled and then drawn on a phase-only SLM. A GPC LS after the SLM maps the phase patterns into intensity (Figure adapted from [15]).

pre-scaled according to Eqn. (27) to optimize the efficiency. GPC results for various optimized images are shown in Fig. 14 together with the unmodulated Gaussian for comparison (Fig. 14(a)).

4.3.2 Dynamic and arbitrarily sized excitation patterns

We now show projection of arbitrary patterns where scaling of the light pattern is not an option, like in biological or optical manipulation experiments. Here $\overline{\alpha}$ is kept at its optimal value by addressing an additional outer phase ring whose radius is given in Eqn. (28). The intensity beyond this radius is considerably lower than that in the utilized region due to the Gaussian roll-off. Results for the ring-compensated neuron-shaped patterns are shown in Fig. 15. Figures 15(d)-(f) show the possibility to optimally illuminate a brain cell that is branching out.

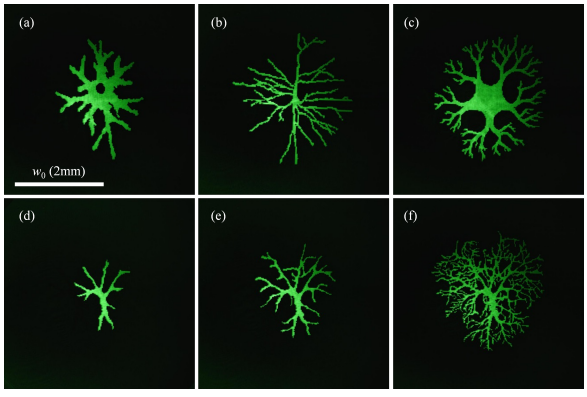

Figure 15: (a)-(c) Experimental results showing GPC generated intensity profiles of various neuron-inspired shapes, directly drawn on an SLM without scaling, but α-compensated by an outer phase ring. (d)-(f) Snapshots from a pattern that is branching out (Figure adapted from [15]).

4.3.3 Efficient illumination of spatial light modulators

A practical application of the GPC light shaper is the efficient illumination of optical devices such as SLMs [40] by properly matching the rectangular active region. To demonstrate this, the output from a GPC light shaper with a 4:3 rectangular phase mask is used to illuminate a phase-only SLM with a 9.9 mm ×7.5 mm active area (Hamamatsu Photonics). The benefits from matched illumination are then demonstrated by encoding computer generated holograms on the SLM for reconstruction with a standard *2f* Fourier transform configuration.

The GPC light shaper used is similar to that used in static experiments in Section 4.2 but having phase mask and PCF designed for 532 nm illumination. The GPC generated 4:3 rectangle was then expanded to match the SLM area. For reference, the GPC LS is disabled by displacing the phase contrast filter (PCF) to generate a Gaussian that is then hard-truncated. This procedure ensures that the input beam will inherently encounter the same potential perturbations along the optical beam path to the SLM and onwards. The laser power for both GPC-enhanced and hard truncated illumination cases are kept at the same level. The reconstructed intensity profiles are then captured by a CCD camera.

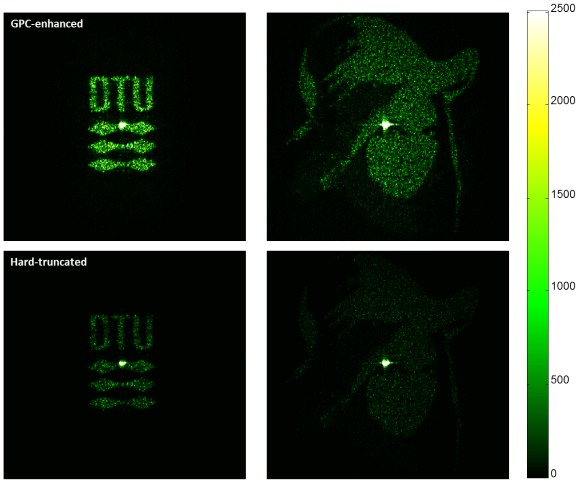

Figure 16: Holographic reconstructions with SLM illumination based on a GPC light shaper (left) and a hard truncated Gaussian (right). Both cases exhibit identical speckle distributions but there is a noticeable gain in intensity for the GPC-enhanced case. Color mappings are adjusted to improve overall contrast (Figure adapted from [40]).

The GPC illuminated hologram on the top row in Fig. 16 shows noticeably much brighter reconstructions with better contrast compared to the bottom row where conventional illumination is used. It is important to note that the aside from brightness and overall efficiency the reconstructed intensities are practically identical for both illumination cases. This means that the same experiments could be done with a 1/3 less powerful laser.

4.4 Summary of single wavelength light shaping experiments

We have experimentally demonstrated a GPC light shaper with Gaussian beams using different phase mask patterns and filtering-configurations designed to give optimal contrast and efficiency for a wide variety of user desired output beam shapes. Results obtained from our analysis simplify the task of implementing GPC light shaping for Gaussian illumination. We demonstrate these with circle, square and rectangle static phase masks and with more complex arbitrary and real-time dynamic shapes using a SLM. Our demonstrations show that a GPC LS could be reused with a fixed PCF in tandem with a variety of interchangeable phase masks and still maintain desired efficiency and gain levels. Experiments show around ~80% efficiency, ~3x intensity gain and ~90% energy savings compared to the commonly implemented hard-truncated expanded Gaussian. The energy saved by using GPC LS makes it attractive for many applications wherein light is best utilized in a particular shape, e.g. rectangles for SLM or display illumination, circles for laser materials processing or even intricate biological patterns found in neurophotonics research.

5 Shaping supercontinuum lasers

5.1 Multi-wavelength light shaping

Many important applications of the interaction of light with matter strongly depend on the illumination wavelength. Hence, for such studies, a laser source containing multiple wavelengths is much more versatile than normal monochromatic lasers. Tabletop supercontinuum light sources have thus been used in a plurality of applications that include optical coherence tomography, spectroscopy, optical characterization or sensing, imaging and microscopy, neuroscience and neurophotonics, and metrology among many others.

Multi-wavelength techniques are invaluable in spectroscopy [41] and provide beneficial enhancements in interferometry [42], both well-established fields whose

significance cannot be overemphasized. Exploiting the wavelength-dependent material response also allows for controlled photo-excitation, targeted monitoring [43], and even simultaneous excitation and monitoring in pump-probe geometries [44].

Light shaping, on the other hand, increases the diversity of such applications by adding spatial control or selectivity to such light-matter interactions. For example, in two-photon optogenetics research [4], one would like to selectively illuminate intricate patterns of dendrites or axons within neurons [2]. As laser sources typically have limited spatial mode patterns, many light shaping approaches have been studied to address different demands such as efficiency, speed, beam quality or economy concerns. Photon efficiency becomes even more important as the high price tag of state-of-the-art laser sources demands an efficient way of managing their available photons. With supercontinuum laser sources, it also becomes important to shape light with consistent output dimensions and efficiency across different wavelengths.

We have previously shown theoretically and numerically that GPC shows robustness to shift in wavelength and can maintain both projection length scale and high efficiency over a range $[0.75\lambda_0;1.5\lambda_0]$ with λ_0 as the characteristic design wavelength [18]. With this performance across multiple wavelengths and the recent availability of tabletop supercontinuum lasers, GPC light shaping opens the possibility for creatively incorporating various multi-wavelength approaches into spatially shaped excitations that can enable new broad-band light applications. Using a supercontinuum laser, we therefore present experiments showing GPC light shaping over a broad wavelength range [19].

5.2 Supercontinuum shaping experiments

5.2.1 PCF and phase mask preparation

The light shaper used is similar to the static GPC-LS in Section 4.2. We chose a design wavelength of 532 nm which is at the center of the visible part of the supercontinuum source. The beam diameter and focal length considered are 1mm and 50 mm, respectively. The phase mask was based on a bitmap image of a globe and is scaled with respect to the input beam diameter such that Eqn. (20) is satisfied.

5.2.2 Optical setup

The setup used for the light shaping with various wavelengths is schematically shown in Fig. 17.

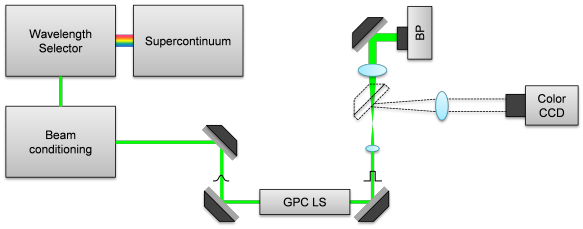

Figure 17: GPC light shaper setup with multi-wavelength illumination. The GPC light shaper (GPC LS) is illuminated with Gaussian beam and with $2w_0 = 1$ mm. The light is passed through a GPC system and then imaged onto a CCD camera or a beam profiler (BP) (Figure adapted from [19]).

The supercontinuum laser (NKT Photonics SuperK) has a 1mm beam diameter. The supercontinuum light goes through a wavelength selector (NKT Photonics SuperK Select) to select the desired wavelength. Output from the wavelength selector was collimated using a fiber delivery system (NKT Photonics SuperK Connect). It should be mentioned that the fiber output beam diameter was slightly wavelength dependent. The beam diameter was close to 1mm at 532 nm and increases with the wavelength. The FWHM of the filtered beam was 1.5 – 4 nm depending on the wavelength. The light was then directed to the GPC LS using relay mirrors that also provided beam alignment. Output from the GPC Light Shaper was magnified (2x) then guided either to a beam profiler (Gentec-EO Beamage 3.0) or to a color CCD.

5.2.3 Results

The efficiencies and energy savings and observable output contrast across different wavelengths were within acceptable experimental variations, indicating the tolerance of the GPC LS. As noted, however, the output beam size was wavelength-dependent and slightly differs from 1 mm which was used in the GPC LS design. This influences measurements making efficiencies lower than expected.

Figure 18 presents globe pattern obtained at different wavelengths. The SuperK power was adjusted for different wavelengths to maintain fairly uniform image brightness on the CCD captures.

These results experimentally verify GPC's robustness to wavelength changes predicted by simulation data from

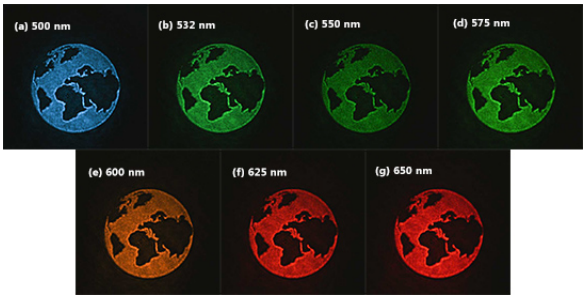

Figure 18: Color CCD images of GPC projections from the same setup, as the wavelength selector is varied from 500 – 650 nm.The power at different wavelengths are adjusted individually for visibility. The input Gaussian beam size exhibits some wavelength dependence (Figure based on results from [19]).

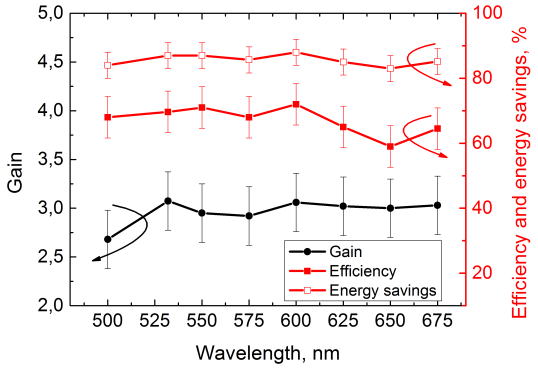

Figure 19: Wavelength dependence of the efficiency, energy savings and gain of a GPC light shaper illuminated with a Gaussian beam. The GPC LS is designed for 532 nm and used a circular phase mask (Figure adapted from [19]).

our previous theoretical analysis [18]. The efficiency, gain and energy savings measurements for different wavelengths were performed at 25 nm wavelength steps while maintaining a small FWHM. Figure 19 shows the experimental data obtained using a circular phase mask. The error bars for the experimental data were obtained from the difference between several measurements at the same wavelength (five on average). These error bars allow room for slight fluctuations caused by the laser beam's intensity and beam size.

The intensity gain was maintained at the level of ~3x throughout the wavelength range. The same ~3x gain level, seen at the red range, which are higher than what simulations predict, can be explained by the slightly larger beam diameter that causes a mismatch of the SRW. This is also consistent with the lowered efficiencies as the SRW mismatch lessens the effect of destructive interference that supposedly defines the dark background. The counteracting effects of gain and efficiency, however, effectively maintains a fairly high energy savings value which are greater than 80%.

6 Summary and outlook

We have reviewed recent GPC developments by presenting the following in this body of work: optimization of GPC for Gaussian illumination; numerical verification and tolerance analysis; experimental verification; GPC's use on illuminating spatial light modulators; GPC's use on efficiently shaping supercontinuum lasers. Our analysis of GPC with Gaussian beams simplifies the design of phase mask and PCF configurations that give optimal contrast and efficiency for a wide variety of user desired patterns. Numerical experiments show that this optimized configurations consistently give ~84% efficiency, ~3x intensity gain and ~93% energy savings compared to the commonly implemented hard truncated expanded Gaussian. Likewise, optical experiments based on the proposed designs show around ~80% efficiency, ~3x intensity gain and ~90% energy savings. The experimental results also indicate robustness, as predicted by the numerical tolerance analysis. With such performance, the GPC LS has thus been tested in practical application scenarios. We demonstrate optimal illumination of a rectangular spatial light modulator. This would allow better response in experiments or increased parallel addressing for e.g. optical sorting, manipulation or opto-electronic switching and for direct laser writing.

Finally, we extend GPC's application to multi-wavelength sources. We verify this new approach using a supercontinuum light source, interfaced with a compact GPC light shaper [15]. With some equipment limitations, GPC light shaping shows ~70% efficiency, ~3x intensity gain, and ~85% energy savings throughout a wavelength range of 500 to 750nm, limited, however, in good agreement with theoretical and numerical predictions. Being the only light shaping technique that can give efficient, speckle-free, high contrast output with arbitrary shapes (to the best of our knowledge), a GPC light shaper combined with a supercontinuum source can be an important enabling tool for biomedical applications. As a static light shaper, GPC can increase the amount of photons directed to rectangular CCDs, hence increasing the brightness and contrast in multispectral imaging. Combined with dynamic SLM's, GPC would bring enable multi-wavelength excitation into biological applications such as neurophotonics or optogenetics.

The energy saved by using a GPC LS therefore makes it attractive for many applications wherein light is best utilized in a particular shape, e.g. rectangles for SLM or display illumination, circles for laser materials processing or even intricate biological patterns found in neurophotonics research. Simple yet effective, a GPC LS could save substantial power in applications in many application that otherwise truncate lasers that truncate lasers to a specific shape.

Acknowledgement: We thank the following for financial support, the Copenhagen Cleantech Cluster (CCC) for GAP, the DTU PoC-Board for Proof-of-Concept funding, and the Enhanced Spatial Light Control in Advanced Optical Fibres (e-space) project by the Danish Council for Strategic Research. We also thank our industrial collaborators, Hamamatsu Photonics K.K., Central Research Laboratory, and NKT Photonics A/S. We also thank Mr. Finn Pedersen for providing technical assistance in building our experimental setups.

References

[1] D. Palima, A. R. Bańas, G. Vizsnyiczai, L. Kelemen, P. Ormos, and J. Glückstad, "Wave-guided optical waveguides," Opt. Express 20, 2004–14 (2012).

[2] E. Papagiakoumou, F. Anselmi, A. Bčgue, V. de Sars, J. Glückstad, E. Y. Isacoff, and V. Emiliani, "Scanless two-photon excitation of channelrhodopsin-2," Nat. Methods 7, 848–854 (2010).

[3] J. G. Lee, B. J. McIlvain, C. J. Lobb, and W. T. Hill, "Analogs of basic electronic circuit elements in a free-space atom chip.," Sci. Rep. 3, 1034 (2013).

[4] E. Papagiakoumou, "Optical developments for optogenetics.," Biol. Cell 105, 443–64 (2013).

[5] D. Palima, C. A. Alonzo, P. J. Rodrigo, and J. Glückstad, "Generalized phase contrast matched to Gaussian illumination," Opt. Express 15, 11971–7 (2007).

[6] A. Bańas, D. Palima, M. Villangca, T. Aabo, and J. Glückstad, "GPC light shaper for speckle-free one- and two- photon contiguous pattern excitation," Opt. Express 7102, 5299–5310 (2014).

[7] T. R. M. Sales, R. P. C. Photonics, C. Road, and R. Ny, "Structured Microlens Arrays for Beam Shaping," in Proc. of SPIE (2003), Vol. 5175, pp. 109–120.

[8] C. Kopp, L. Ravel, and P. Meyrueis, "Efficient beamshaper homogenizer design combining diffractive optical elements, microlens array and random phase plate," J. Opt. A Pure Appl. Opt. 1, 398–403 (1999).

[9] J. A. Hoffnagle and C. M. Jefferson, "Design and performance of a refractive optical system that converts a Gaussian to a flattop beam.," Appl. Opt. 39, 5488–99 (2000).

[10] S. K. Case, P. R. Haugen, and O. J. Lřkberg, "Multifacet holographic optical elements for wave front transformations.," Appl. Opt. 20, 2670–5 (1981).

[11] I. Gur and D. Mendlovic, "Diffraction limited domain flat-top generator," 237–248 (1998).

[12] W. B. Veldkamp, "Laser beam profile shaping with interlaced binary diffraction gratings.," Appl. Opt. 21, 3209–12 (1982).

[13] M. R. Wang, "Analysis and optimization on single-zone binary flat-top beam shaper," Opt. Eng. 42, 3106 (2003).

[14] R. Voelkel and K. J. Weible, "Laser beam homogenizing: limitations and constraints," in Proc. of SPIE, A. Duparré and R. Geyl, eds. (2008), Vol. 7102, p. 71020J–71020J–12.

[15] A. Bańas, O. Kopylov, M. Villangca, D. Palima, and J. Glückstad, "GPC light shaper: static and dynamic experimental demonstrations," Opt. Express (2014).

[16] J. Glückstad and P. C. Mogensen, "Optimal phase contrast in common-path interferometry.," Appl. Opt. 40, 268–82 (2001).

[17] S. Tauro, A. Bańas, D. Palima, and J. Glückstad, "Experimental demonstration of Generalized Phase Contrast based Gaussian beam-shaper," Opt. Express 19, 7106–11 (2011).

[18] D. Palima and J. Glückstad, "Multi-wavelength spatial light shaping using generalized phase contrast," Opt. Express 16, 1331–42 (2008).

[19] O. Kopylov, A. Bańas, M. Villangca, and D. Palima, "GPC light shaping a supercontinuum source," 23, 1894–1905 (2015).

[20] A. W. Lohmann and D. P. Paris, "Binary fraunhofer holograms, generated by computer.," Appl. Opt. 6, 1739–48 (1967).

[21] W. H. Lee, "Sampled fourier transform hologram generated by computer," Appl. Opt. 9, 639–43 (1970).

[22] J. Glückstad and D. Z. Palima, Generalized Phase Contrast: Applications in Optics and Photonics (Springer Series in Optical Sciences, 2009).

[23] D. G. Grier, "A revolution in optical manipulation," Nature 424, 810–6 (2003).

[24] M. A. Go, C. Stricker, S. Redman, H.-A. Bachor, and V. R. Daria, "Simultaneous multi-site two-photon photostimulation in three dimensions.," J. Biophotonics 5, 745–53 (2012).

[25] L. Ge, M. Duelli, and R. Cohn, "Enumeration of illumination and scanning modes from real-time spatial light modulators.," Opt. Express 7, 403–16 (2000).

[26] T. Matsuoka, M. Nishi, M. Sakakura, K. Miura, K. Hirao, D. Palima, S. Tauro, A. Bańas, and J. Glückstad, "Functionalized 2PP structures for the BioPhotonics Workstation," in Proceedings of SPIE, D. L. Andrews, E. J. Galvez, and J. Glückstad, eds. (2011), Vol. 7950, p. 79500Q.

[27] P. J. Rodrigo, L. Gammelgaard, P. Břggild, I. Perch-Nielsen, and J. Glückstad, "Actuation of microfabricated tools using multiple GPC-based counterpropagating-beam traps.," Opt. Express 13, 6899–904 (2005).

[28] Y. Tanaka, S. Tsutsui, M. Ishikawa, and H. Kitajima, "Hybrid optical tweezers for dynamic micro-bead arrays.," Opt. Express 19, 15445–51 (2011).

[29] S. Tauro, A. Bańas, D. Palima, and J. Glückstad, "Dynamic axial stabilization of counter-propagating beam-traps with feedback control," Opt. Express 18, 18217–22 (2010).

[30] P. J. Rodrigo, V. R. Daria, and J. Glückstad, "Real-time three-dimensional optical micromanipulation of multiple particles and living cells.," Opt. Lett. 29, 2270–2 (2004).

[31] J. Glückstad, L. Lading, H. Toyoda, and T. Hara, "Lossless light projection.," Opt. Lett. 22, 1373–5 (1997).

[32] V. Nourrit, J.-L. de Bougrenet de la Tocnaye, and P. Chanclou, "Propagation and diffraction of truncated Gaussian beams," J. Opt. Soc. Am. A 18, 546 (2001).

[33] R. W. Gerchberg and W. O. Saxton, "A practical algorithm for the determination of the phase from image and diffraction plane pictures," Optik (Stuttg). 35, 237–246 (1972).
[34] A. Bańas, D. Palima, and J. Glückstad, "Matched-filtering generalized phase contrast using LCoS pico-projectors for beam-forming.," Opt. Express 20, 9705–12 (2012).
[35] J. Glückstad and P. C. Mogensen, "Reconfigurable ternary-phase array illuminator based on the generalised phase contrast method," 169–175 (2000).
[36] F. Kenny, F. S. Choi, J. Glückstad, and M. J. Booth, "Adaptive optimisation of a generalised phase contrast beam shaping system," Opt. Commun. 342, 109–114 (2015).
[37] R. Porras-Aguilar, K. Falaggis, J. C. Ramirez-San-Juan, and R. Ramos-Garcia, "Self-calibrating common-path interferometry," Opt. Express 23, 3327 (2015).
[38] V. Daria, J. Glückstad, P. C. Mogensen, R. L. Eriksen, and S. Sinzinger, "Implementing the generalized phase-contrast method in a planar-integrated micro-optics platform.," Opt. Lett. 27, 945–7 (2002).
[39] D. Palima and J. Glückstad, "Gaussian to uniform intensity shaper based on generalized phase contrast," Opt. Express 16, 1507–16 (2008).
[40] M. Villangca, A. Bańas, O. Kopylov, D. Palima, and J. Glückstad, "Optimal illumination of phase-only diffractive element using GPC light shaper," in Proc. of SPIE (2015), pp. 9379–24.
[41] E. Cerussi, D. Jakubowski, N. Shah, F. Bevilacqua, R. Lanning, a J. Berger, D. Hsiang, J. Butler, R. F. Holcombe, and B. J. Tromberg, "Spectroscopy enhances the information content of optical mammography," J. Biomed. Opt. 7, 60–71 (2002).
[42] Y. Y. Cheng and J. C. Wyant, "Multiple-wavelength phase-shifting interferometry," Appl. Opt. 24, 804 (1985).
[43] E. L. Heffer and S. Fantini, "Quantitative oximetry of breast tumors: a near-infrared method that identifies two optimal wavelengths for each tumor," Appl. Opt. 41, 3827–3839 (2002).
[44] Y.-C. Chen, N. R. Raravikar, L. S. Schadler, P. M. Ajayan, Y.-P. Zhao, T.-M. Lu, G.-C. Wang, and X.-C. Zhang, "Ultrafast optical switching properties of single-wall carbon nanotube polymer composites at 1.55 μm," Appl. Phys. Lett. 81, 975 (2002).